IEEE Access
Multidisciplinary | Rapid Review | Open Access Journal

Received June 14, 2021, accepted June 29, 2021, date of publication July 8, 2021, date of current version July 16, 2021.

Digital Object Identifier 10.1109/ACCESS.2021.3095619

Manifestation of Flexural Vibration Modes of Rails by the Phase-Based Magnification Method

HYUNGJUN KIM[1], YOUNGBEEN CHUNG[1], JIE JIN[2], AND JUNHONG PARK[1], (Member, IEEE)
[1]Department of Mechanical Engineering, Hanyang University, Seoul 04763, Republic of Korea
[2]School of Electromechanical and Automotive Engineering, Yantai University, Yantai 264005, China

Corresponding author: Junhong Park (parkj@hanyang.ac.kr)

This work was supported by the Basic Science Research Program through the National Research Foundation of Korea (NRF) funded by the Ministry of Education, Science and Technology under Grant NRF-2019R1A2C100561912.

ABSTRACT With the recent development of high performance photography devices, vibration measurements using digital image processing can be utilized for the condition monitoring and the analysis of generation mechanisms. High-quality image recording provides very dense spatial information unlike physical sensors with a limited number of point-oriented measurements and output channels such as accelerometers. Moreover, image acquisition is a non-contact technique and ensures that the installed sensors do not affect the mass or stiffness. In this study, the vibration mode of rails is investigated using the phase-based video magnification method. An extensive amount of information that cannot be detected by human eyes, can be obtained with this imaging motion magnification technique by amplifying and visualising the minute vibrational movements. Flexural vibration modes in rails generate rolling noise, especially at high frequencies where the displacement amplitudes are small. The motion magnification method is applied using a high-speed camera to measure the rail mode shapes. The measured mode shapes are compared to the numerical results obtained from the waveguide finite element method. This method helps in understanding the vibration generation and the transfer mechanisms in the waveguide structures with a uniform cross-section in the lengthwise direction such as a railway track.

INDEX TERMS Phase-based motion magnification, railway track, waveguide finite element method.

I. INTRODUCTION

The modal analysis of structures is performed using the data obtained from the sensors attached discretely to vibrating structures. Contact accelerometers are commonly used for modal analysis and provide precise information about the vibrational mechanisms. During vibration tests, sensors such as accelerometers, strain gauges, or linear variable differential transformers must be applied to the mechanical structures without minimal mass and stiffness loading. The local variations sometimes produce a considerable influence that can be confused with the system characteristics [1]. When accelerometers are used for vibration measurements, the mechanical impedance must be analyzed for modal estimations [2], [3]. Non-contact measurement methods are advantageous in the case of minimal structural loading on systems under tests. The vibration characteristics provide detailed information about the vibration generation, transmission, and structural integrity, when identified using images.

The use of images obtained from digital video cameras can be considered as a non-contact approach in structural measurements [4]–[7]. Optical measurement methods such as digital image correlation (DIC) and point tracking (PT) have been utilized to perform modal analysis on large-scale industrial structures [8]–[11]. The DIC and PT methods provide smooth mode shapes with high accuracy. These methods utilize speckle patterns or markers painted on the surface of the structure.

The motion magnification method [12]–[18] has recently gained attention in structural motion estimation and system dynamics identification. These methods do not require surface perpetrations or reduction in the size data. There are two methods of revealing minute motions invisible to the naked eye, which differ based a metaphor in fluid dynamics.

The associate editor coordinating the review of this manuscript and approving it for publication was Zahid Akhtar.

In the Lagrangian perspective, the movement of fluid particles is tracked over time. The points in the scene are tracked and the pixel colours are added throughout the frame corresponding to the magnified motion vectors [12]. Conversely, the Eulerian perspective considers a fixed reference frame and exhibits fluid properties over time at each fixed location [13], [14].

Wu *et al.* [13] followed the approach of linear Eulerian video magnification (EVM) by considering the time series of intensity values at each pixel independently, and amplifying the temporal variations in a frequency band of interest to produce a motion magnified video. Remarkably, this simple method of considering only the colour changes at each pixel was used to manipulate small motions. The colour changes were linked through a first-order Taylor series expansion. This method was fast and robust, eliminating the need for expensive flow computation. Because linear EVM [13] relies on a first-order Taylor expansion, it supports small magnification factors. When the magnification factor is large, the noise is amplified as well.

An improved video magnification method was introduced by Wadhwa *et al.* [14]. The small motion in the video is magnified by multiplying a magnification factor to the phase difference of the images between the frames in the phase-based magnification (PBM) method [14]. Unlike the noise of the video being equally amplified after applying the EVM method, the use of the PBM method exhibits less sensitivity to noise during the magnification of the video owing to which the PBM method has been used in engineering applications. To identify the natural mode shape of the structure, the theoretical or the numerical analysis of the vibration behavior based on the geometric and dynamic parameters is required. This method provides a solution for the mode shapes of the structures. Wadhwa *et al.* [14] proposed applications of the PBM method in engineering fields. Chen *et al.* measured the mode shapes of beams [19], [20] and pipes [20] using the PBM method. The deformation shapes of the blades have also been observed by Sarrafi *et al.* [21]. Civera *et al.* [19] used the PBM method to assess the health of a beam by monitoring the cracks. Therefore, this method can be useful in measuring the dynamic behavior of the cross-section of complex structures such as rails.

The 3D finite element (FE) model can be used to analyze the dynamic characteristics of a railway track [22]–[24], but since the FE method involves high computational costs, the use of either the semi-analytical finite element or the waveguide finite element (WFE) method has been proposed for wave analysis [25]–[27]. These methods use the 2D cross-sectional model of the waveguide structure to analyze the 3D behavior. The WFE method, also known as the 2.5D FE method has been widely used in the vibration analysis of waveguide structures such as car tyres [28], rails [29]–[32], and plates [33]–[38]. Nilsson *et al.* [29] presented the wave types of rails to identify the particular wave which generates the sound radiation. Ryue *et al.* studied the propagation of the waves along the rail track [30] and evaluated the decay rate [31]. The vertical bending wave radiates most of the rail noise above 5 kHz [32]. The lateral bending wave along with the torsional first and second web bending waves contribute to the noise below 5 kHz. The wave types were analyzed numerically and confirmed from the resonance of the vibration and the sound radiation. Therefore, the validation of the mode shapes of the rail using actual measurements is still required.

This study applies phase-based motion magnification method to measure the vibration modes of complex-shaped structures such as rails. In previous studies, simple rectangular (beam) and circle (pipe) shapes were used for verifications, and the frequency band for the magnification required in the PBM method was selected priori. In the case of the rail used in this study, the vibration modes appear from simultaneous wave propagations in complex-shaped cross-section. Typically, a dispersion diagram is used to find the resonance frequencies and the mode shapes of the rail. The frequency bands for the rail used in the experiment were selected with the help of a dispersion diagram based on the wave propagation characteristics of the infinite-length rail identified by the WFE method. The mode shape of the rail was derived by applying the PBM method in the selected frequency bands for the recorded video. The measurements of the mode shape of the rail were validated by comparing the results of the PBM and the WFE methods.

II. WAVEGUIDE FINITE ELEMENT METHOD

The WFE method was used in this study to predict the vibration modes of the rail. This section briefly describes the WFE method, which is known to be particularly useful for waveguide structures which have a uniform cross-section along the lengthwise direction, such as rails [29]–[32], plates [33]–[38], pipes, and ducts. The method was applied to predict the vibration and sound radiation of waveguide structures [28], [29]. In this study, the wavenumber domain analysis [39] was used to predict the vibration behavior of the rail.

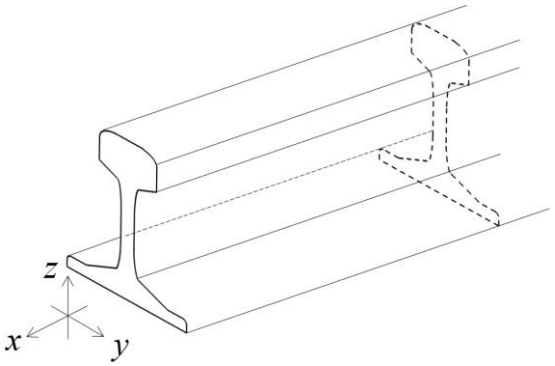

FIGURE 1. Coordinates and scheme of a railway track.

In the wavenumber domain analysis method, only a two-dimensional cross-section of the structure is meshed, assuming harmonic dependence on time and on the third direction in space, as indicated in Fig. 1. The governing

equation of the WFEs for a waveguide structure analyzed with plate elements is given by

$$\left[\mathbf{K}_s(\kappa) - \omega^2 \mathbf{M}_s\right]\tilde{\mathbf{\Phi}} = \tilde{\mathbf{F}}_s \tag{1}$$

where $\tilde{\mathbf{\Phi}}$ is the nodal displacement vector in the wavenumber domain, ω is the angular frequency, and κ is the structural wavenumber along the x direction. The stiffness matrix was derived as follows:

$$\mathbf{K}_s(\kappa) = \left(\mathbf{K}_{s4}(-\mathrm{i}\kappa)^4 + \mathbf{K}_{s2}(-\mathrm{i}\kappa)^2 + \mathbf{K}_{s1}(-\mathrm{i}\kappa) + \mathbf{K}_{s0}\right) \times (1 + \mathrm{i}\eta_s), \tag{2}$$

in which $\mathbf{K}_{s4}$, $\mathbf{K}_{s2}$, $\mathbf{K}_{s1}$, and $\mathbf{K}_{s0}$ are related to the stiffness of the structure and η_s is the damping loss factor (which may be frequency-dependent). $\mathbf{M}_s$ is the mass matrix, and $\tilde{\mathbf{F}}_s$ represents the excitation forces at the nodes. For free vibration analysis, i.e., $\tilde{\mathbf{F}}_s = \mathbf{0}$ and $\eta_s = 0$, equation (2) was solved for ω at the given real wavenumbers. This eigenvalue problem provides the dispersion relations of waves propagating along the lengthwise direction of the structure.

A. MODELLING THE RAILWAY TRACK

To estimate the wave propagations, a standard UIC60 rail was examined by the WFE analysis. Only the rail for the free boundary condition was considered to neglect the effects of the sleeper, ballast, and railpad. The cross-sectional model of the rail structure is illustrated in Fig. 2. The model was composed of eight-noded solid elements with a quadrilateral shape function. For the tested rail, the mass per unit length was 60.3 kg/m, Young's modulus was 210 GPa, and Poisson's ratio was 0.3. The model consists of 341 nodes and 86 elements.

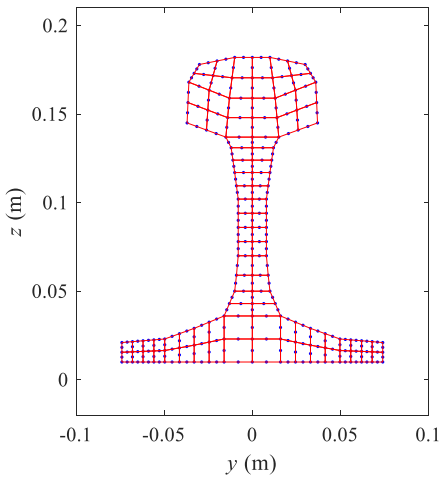

FIGURE 2. Numerical elements in cross-section used in WFE analysis.

B. DISPERSION RELATION FOR THE INFINITE-LENGTH RAILWAY TRACK

The dispersion diagram obtained from WFE models of the rails, as illustrated in Fig. 3 and Fig. 4, helps in understanding the wave propagation characteristics along the rail.

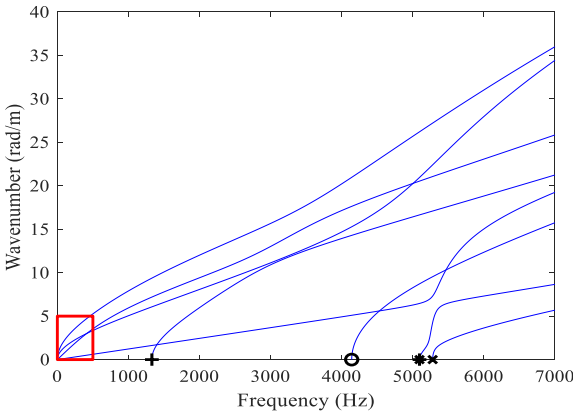

FIGURE 3. Dispersion diagrams of the infinite length railway track.

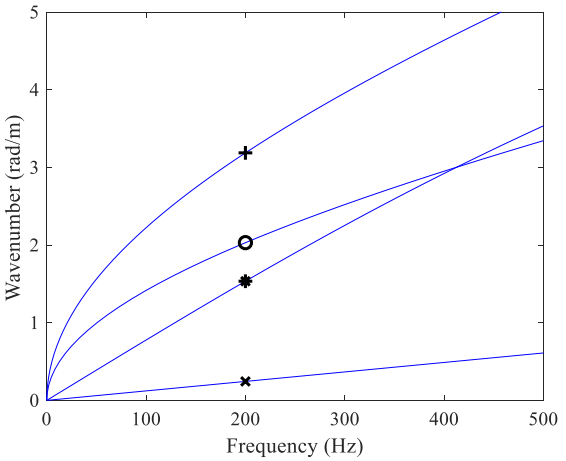

FIGURE 4. Dispersion diagrams of the infinite length railway track magnified between 0 and 500 Hz.

The wavenumbers from 0 to 40 rad/m with the corresponding frequencies were identified from the eigenvalue analysis of (1).

Fig. 3 shows four waves at low frequency (below 1 kHz). The magnified diagram of Fig. 3 is plotted in Fig. 4. At a fixed frequency of 200 Hz, the cross-sectional deformations of the four waves marked in Fig. 4 are shown in Fig. 5. The vibration originates from the lateral bending waves of the rail at 3.19 rad/m (marked with '+'). Conversely, the vertical bending waves of the rail appear at 2.03 rad/m (marked with '◯'). The deformation shape of the wave marked with '∗' shows the torsion wave mode. The longitudinal waves are observed at a lower wavenumber of 0.24 rad/m (marked with '×').

At high frequencies, between 1 and 7 kHz, four waves start to appear (0 rad/m). These waves correspond to the localized waves, and their cross-sectional deformations (marked with '+' at 1330 Hz, '◯' at 4141 Hz, '∗' at 5095 Hz and '×' at 5280 Hz in Fig. 3) are shown in Fig. 6. These wave modes are the first web bending wave (Fig. 6(a)), second web bending

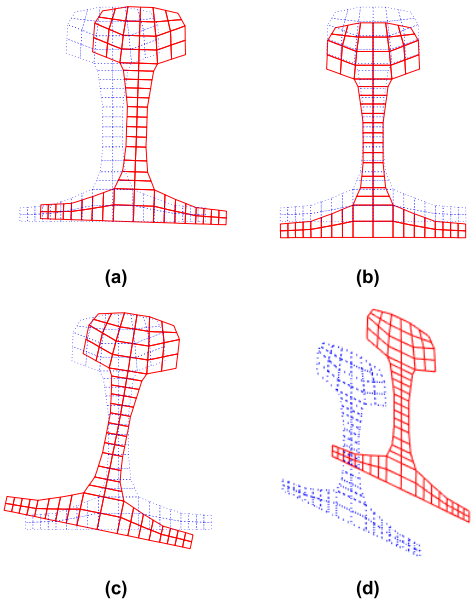

FIGURE 5. Deformation shapes of the wave chosen in Fig. 4. (a) '+' at 3.19 rad/m, (b) '○' at 2.03 rad/m, (c) '∗' at 1.53 rad/m and (d) '×' at 0.24 rad/m, at fixed 200 Hz.

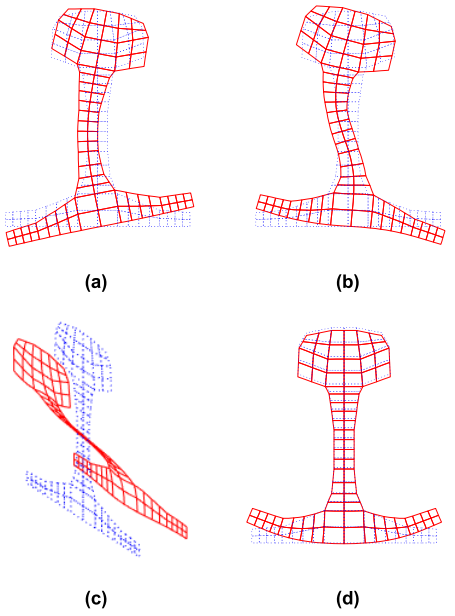

FIGURE 6. Deformation shapes of the wave chosen in Fig. 3. (a) '+' at 1330 Hz, (b) '○' at 4141 Hz, (c) '∗' at 5095 Hz and (d) '×' at 5280 Hz, at fixed 0 rad/m.

wave (Fig. 6(b)), second longitudinal wave (Fig. 6(c)) and flapping wave modes of the rail foot (Fig. 6(d)).

These vibration modes have been analyzed numerically in previous studies using FEM [24] or WFEM [32]. However, only predictions based on numerical analysis have been reported, and no actual instrumentation of these mode features has been performed in those studies. Although the responses of the rail, such as the point receptance or the mobility, can be calculated and compared to the measured results, there is a limit to the vibration modes that can be inferred from the point responses. The vibration mode must be initially verified since the effects on the vibration and the noise characteristics of the rail vary depending on the characteristics of the modes.

III. PHASE-BASED MAGNIFICATION METHOD

This section presents the PBM method. This method has been applied in engineering fields to visualize small motions of structures, which are almost undetectable by human eyes. These applications include analysis of small vibrations of beams [19], pipes [18], [20] and blades [21], [40]. Only a brief overview of this method is provided here since a detailed explanation of this method can be found in the literature [14], [17].

A. BASIC CONCEPT OF THE PHASE-BASED MAGNIFICATION METHOD

The basic concept of the PBM method involves the translation of motion over time with the phase shift of the image profile using the Fourier series decomposition. When one-dimensional image intensity at time t, is defined by $I(x, t)$, the intensity of the image with a small translation of $\delta(t)$ is expressed as $I(x + \delta(t))$ using a sum of the sinusoids as

$$I(x + \delta(t)) = \sum_{\omega=-\infty}^{\infty} A_\omega e^{i\omega(x+\delta(t))} \tag{3}$$

At time t_0, $\delta(t_0) = 0$, and the intensity of the reference frame, $I_0(x)$, is expressed as follows:

$$I_0(x) = \sum_{\omega=-\infty}^{\infty} A_\omega e^{i\phi(x)} \tag{4}$$

where $\phi(x) = \omega x$. Magnifying this phase difference by a factor, α and using it to shift the Fourier coefficients of $I(x + \delta(t))$ yields a new image sequence in which the translations have been exactly magnified, which can be represented as follows:

$$I(x + (1 + \alpha)\delta(t)) = \sum_{\omega=-\infty}^{\infty} A_\omega e^{i\phi(x)} e^{i\omega(1+\alpha)\delta(t)} \tag{5}$$

Motions to be magnified in a video are generally local. The details of the complex steerable pyramid are stated in Sec. 3.2 and the entire process of the PBM is shown in Fig. 7. The images in a video are decomposed using the complex steerable pyramid to amplify the local motion in the images [41], [42]. In this process, the images of the amplitudes and phases corresponding to the local motion are separated, and the images of the phases are extracted using a frequency band-passed filter. The band-passed phase is amplified by the magnification factor, and the video is reconstructed.

B. MAGNIFICATION OF LOCAL TRANSLATION USING COMPLEX STEERABLE PYRAMID

The complex steerable pyramid [41], [42], which is a type of the image filter, is a complex, overcomplete, linear transform.

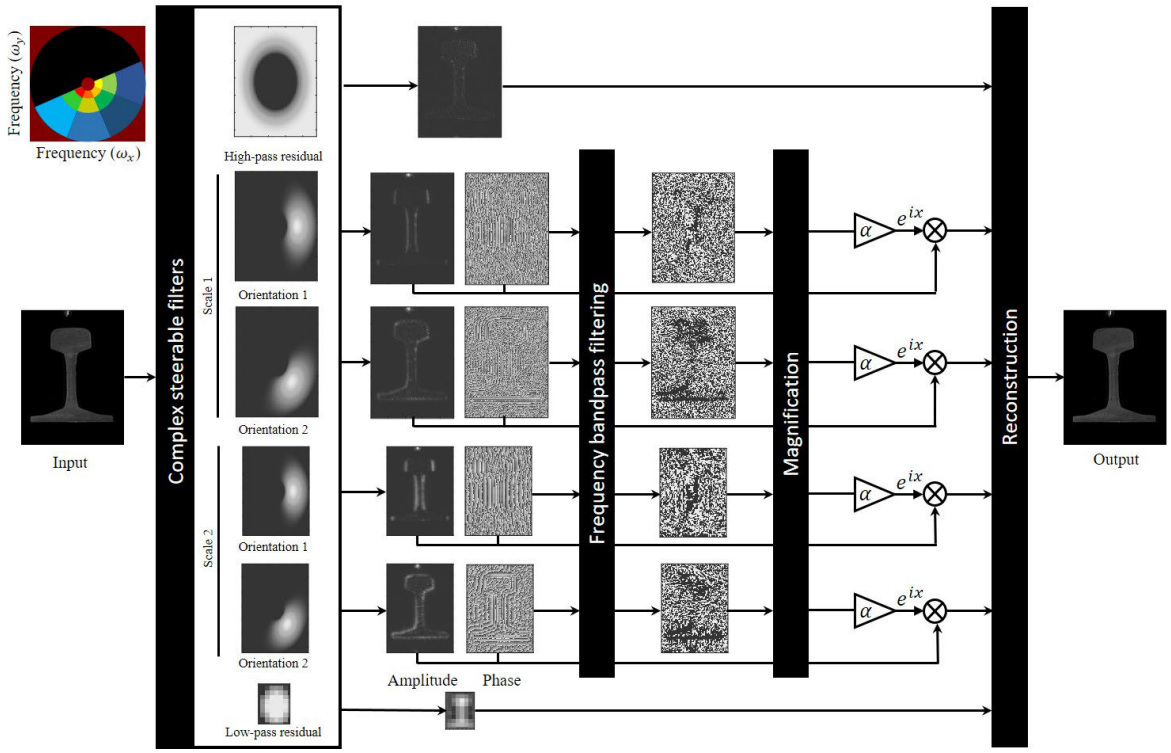

FIGURE 7. Phase-based magnification process.

Instead of a single Laplacian or a Gaussian filter, it uses a bank of filters that are steerable at each level of the pyramid. It decomposes a single channel image, $I(x, y)$, into a set of coefficients corresponding to basis functions that are simultaneously localized in the position (x, y), the spatial scale (r), and the orientation (θ). The image is reconstructed by multiplying the coefficients by the basis functions and the summation.

Through this filter, a Gaussian window multiplied by a complex sinusoid, was used as a basis function to extract the phase component for the image intensity. The Gabor wavelet, which is the Gaussian envelope of the trigonometric functions with real and imaginary parts, can be expressed as follows:

$$\psi_r(x) = e^{-\frac{x^2}{2\sigma^2}} e^{-i\omega x}, \tag{6}$$

In the complex steerable pyramid, the basis functions are self-similar. The ratio between σ and ω, which is determined by the scale, r (the orientation, θ, is not considered in 1D), has a fixed value. For the image decomposition, the frames of the one-dimensional image are convoluted with the complex Gabor filter, $\psi(x)$ as follows:

$$L_r(x) = I(x) * \psi_r(x), \tag{7}$$

where L_r refers to the image intensity after convolution by the Gabor filter. The new image intensity at t and t_0 is expressed by

$$L_r(x, t_0) = \int_{-\infty}^{\infty} I(x' - x)\, e^{-\frac{x'^2}{2\sigma^2}} e^{-i\omega x'} dx', \tag{8}$$

$$L_r(x, t) = \left(\int_{-\infty}^{\infty} I(x' + \delta(t) - x)\, e^{-\frac{(x'+\delta(t))^2}{2\sigma^2}} e^{-i\omega x'} dx' \right) \cdot \left(e^{-i\omega\delta(t)} \right) \tag{9}$$

In (8) and (9), the phases of the frame at t and t_0 are defined by

$$\phi(x', t_0) = \arg[L_r(x, t_0)], \tag{10}$$

$$\phi(x', t) = \arg[L_r(x, t)], \tag{11}$$

The phase difference between the frames at t and t_0 is calculated as follows:

$$\Delta\phi = \phi(x', t) - \phi(x', t_0) = \omega\delta(t), \tag{12}$$

In (12), the phase difference is proportional to the translation, and $\alpha\omega\delta(t)$ is the magnified phase difference for magnifying the motion. The magnified image intensity is then expressed as

$$L_{m,r}(x, t) = \left(\int_{-\infty}^{\infty} I(x' + (1+\alpha)\delta(t) - x) \times e^{-\frac{(x'+(1+\alpha)\delta(t))^2}{2\sigma^2}} e^{-i\omega x'} dx' \right) \cdot \left(e^{-i\omega(1+\alpha)\delta(t)} \right), \tag{13}$$

The magnification factor α is satisfied as follows

$$\alpha\delta\left(t\right) < \sigma, \tag{14}$$

in the octave-bandwidth steerable pyramid.

When expanding the Gabor wavelet in two dimensions, equation (6) is expressed by $\psi_{r,\theta}\left(x, y\right)$, thereby introducing the orientation, θ. It corresponds to the spatial scale, (r), and orientation, (θ), and is known as the complex steerable filter. The image intensity in two dimensions, using the complex steerable pyramid, is expressed by

$$L_{r,\theta}\left(x, y\right) = I\left(x, y\right) * \psi_{r,\theta}\left(x, y\right), \tag{15}$$

To reconstruct the image after magnification by obtaining the phase difference and calculating the argument difference between complex values, the basis functions are convolved with $L_{r,\theta}\left(x, y\right)$ and summated for each of the scales and the orientations as follows:

$$I_R\left(x, y\right) = \sum_{r,\theta} L_{r,\theta} * \psi_{r,\theta} = I\left(x, y\right) * \left(\sum_{r,\theta} \psi_{r,\theta} * \psi_{r,\theta}\right), \tag{16}$$

C. FREQUENCY BAND FOR THE MAGNIFICATION

To magnify the motion in the video using the PBM method, the frequency band where the motion appears dominantly should be determined. The measurements of time and frequency responses are useful for the identification of resonance frequencies so that they help decide frequency band. In this study, however, it is focused on the decision of the frequency band without contact accelerometers. If the wavenumber of the rail is determined, the frequency is obtained from the dispersion diagram. The rail used in the measurement has a length of 1.4 m, and its allowed wavenumbers are calculated from $\kappa_n = n\pi/l$. If there are several waves in a frequency band requiring motion magnification, the modes overlap. Therefore, it is necessary to include only a single wave in the frequency band. However, the wave with the lowest wavenumber (the longest wavelength) at $\kappa_1 = 2.24$ rad/m is considered because the largest motions of each mode shape appear at the first mode in the lengthwise direction, and the higher wave modes have much smaller effects.

The dispersion diagrams derived for the infinite and the finite length rails are shown in Fig. 8 and the magnified ones are shown in Fig. 9. The center frequencies corresponding to each wave mode shown in Figs 8 and 9 are listed in Table 1. The frequency bands for magnification were set as 10 Hz with respect to the center frequencies.

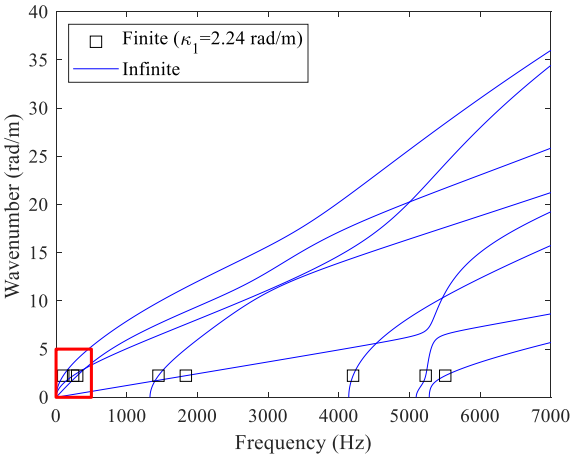

FIGURE 8. Dispersion diagrams of the infinite and finite (κ_1 = 2.24 rad/m) length railway tracks.

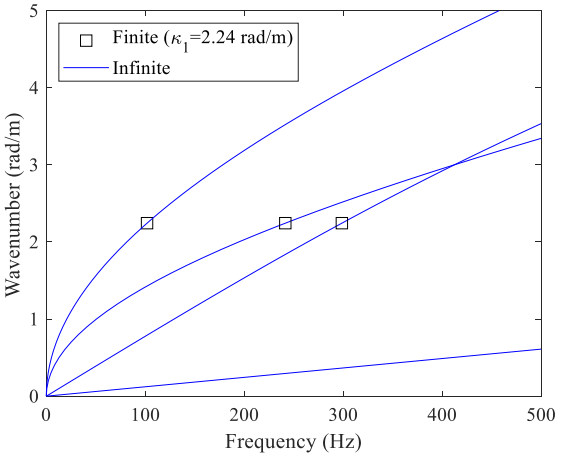

FIGURE 9. Dispersion diagrams of the infinite and finite (κ_1 = 2.24 rad/m) length railway tracks magnified between 0 and 500 Hz.

TABLE 1. Center frequency for the band-passed filter used in the magnification.

Type	Wave mode	Center frequency (Hz)
Symmetric motion	Vertical bending wave	242
	Flapping wave of the rail foot	5230
Anti-symmetric global motion	Lateral bending wave	102
	Torsion wave	300
Anti-symmetric local motion	First web bending wave	1410
	Second web bending wave	4200
Longitudinal motion	First longitudinal wave	1840
	Second longitudinal wave	5480

IV. VISUALIZED VIBRATION MODES OF THE RAIL

A. EXPERIMENTAL SETUP

Fig. 10 illustrates the experimental setup to measure the vibration modes of the rail. The rail is 1.4 m long and hangs freely on both edges with elastic ropes. For the measurement of the vertical and the lateral transverse waves, a high-speed camera (MEMRECAM GX-8F) is used to record the cross-section of the rail, as shown in Fig. 10(a). In addition, the camera records the side of the rail to measure the longitudinal deformations, as shown in Fig. 10(b). The rail cross-section is recorded with a frame rate of 30000 FPS at a resolution of 240 × 288 to examine vibration mechanism in the high frequency range, up to 7 kHz.

(a)

(b)

FIGURE 10. Experimental setup for measuring (a) the vertical and lateral bending waves and (b) longitudinal waves of the railway track.

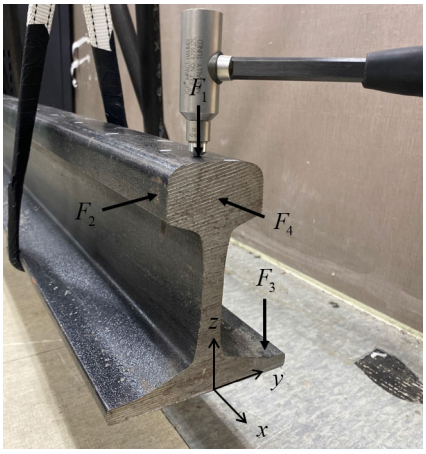

FIGURE 11. Position of impact force excitation on the rail specimen.

Fig. 11 shows the excitation location on the rail using an impact hammer. The rail heads in the z-direction (F_1), side (F_2), right rail foot (F_3), and center of the rail head cross-section (F_4) were excited, respectively. The excitation force locations were varied to induce deformation of the corresponding modes without influence from the other modes.

B. MODE SHAPES OF THE RAIL USING THE PHASE-BASED MOTION MAGNIFICATION

The mode shapes of the rail were identified by applying the PBM method, described in Sec. 3. The frequency bandpass filters listed in Table 1 in Sec. 3.3 are applied for the magnification. The octave steerable pyramid filter, which consists of 4 orientations, octave bandwidth, 18 filters, is used in this study because it takes less computational costs than other type of filters.

The vertical bending wave and the flapping mode wave of the rail foot are generated by the vertical excitation. Since both waves shows symmetric deformations, the excitation with the hammer perpendicular to the center of the rail head (F_1) is used to measure these modes. The deformation identified by the vertical bending wave is shown in Video 1 and that of the flapping mode wave is shown in Video 2 (included in the supplements). Videos 1 and 2 were recorded at a play rate of 60 and 5 FPS, respectively. The magnification factors are 500 for Video 1 and 8000 for Video 2. Fig. 12 shows the frames where the largest deformations appear. The vertical bending and the flapping modes are observed clearly. Although the input images are identical, different mode shapes are observed because only the motions of the different frequency bands are magnified.

To measure the lateral bending and the torsion waves, a point force with the hammer is applied on the rail head in the lateral direction (F_2). The measured result of the lateral bending wave is shown in Video 3 and that of the torsional wave is shown in Video 4. Videos 3 and 4 were recorded at a rate of 120 and 60 FPS, respectively. The magnification factors are 100 for Video 3 and 2000 for Video 4. Fig. 13 shows the frames with the largest deformations. The lateral bending wave and the torsion wave have been clearly identified, which was not possible with the conventional methods of vibration measurement. The force from the operating trains is applied to the rail in oblique directions due to the inclined contact positions between the rail and the wheels. The lateral modes are generated from this oblique excitation, which contributes significantly to the generation of rolling noise [29]. In addition to the predicted behavior, the measurements of the vibration shapes presented in these figures provide important information required for the reduction of the rolling noise.

A force is applied on the rail foot (F_3) to measure the first and the second web bending waves because the rail foot deforms largely in these modes, as shown in Fig. 6. The measured results for these two modes are shown in Videos 5 and 6 with recorded play rates of 20 and 5 FPS. The magnification factors are 5000 for Video 5 and 10000 for Video 6. Fig. 14 shows the frames with the largest deformations and the first and the second web bending waves are observed. Both modes are observed with smaller magnitude deformations when compared to those of the vertical and the lateral wave motions. Although the vibration magnitudes are small, the vibration mechanism induces large deviations in the cross-sectional shape and causes the large strain energy

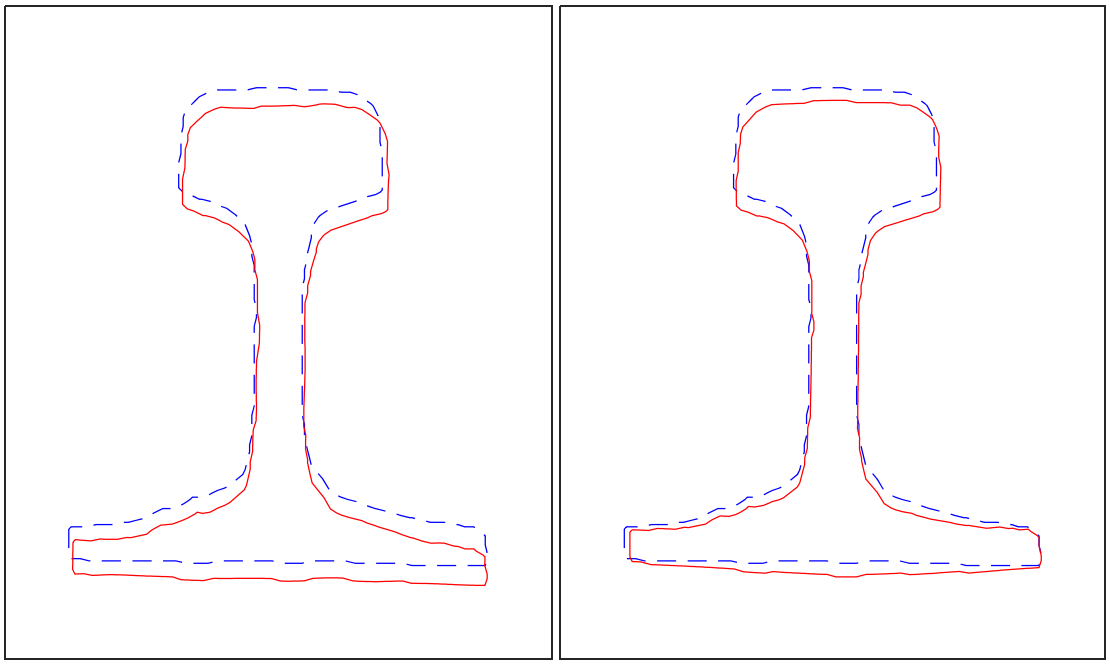

FIGURE 12. Measured results of (a) the vertical bending and (b) flapping wave modes of the rail derived from the PBM.

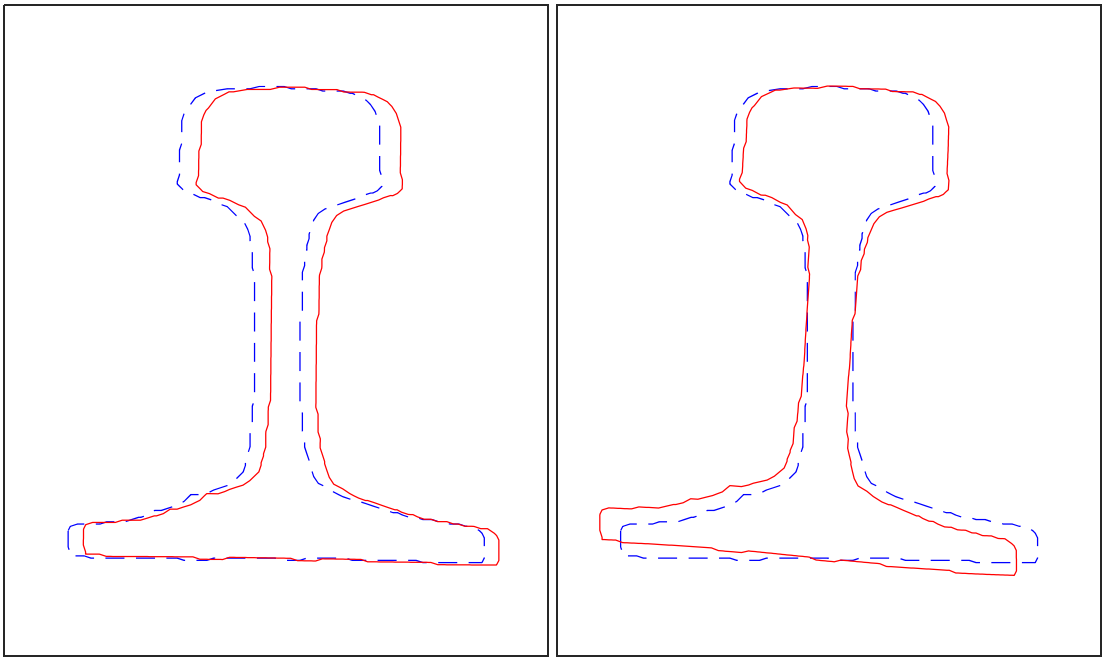

FIGURE 13. Identified cross sectional deformation of the vibration modes by (a) the lateral bending and (b) torsion waves from the PBM.

transfer along the rails. The large strain energy generation on the rail induces dynamic fatigue failure when exposed to excessive vibrations.

When a force is applied in the longitudinal direction (F_4), the vibrations in the corresponding mechanism are generated dominantly. Videos 7 and 8 shows the measured results for

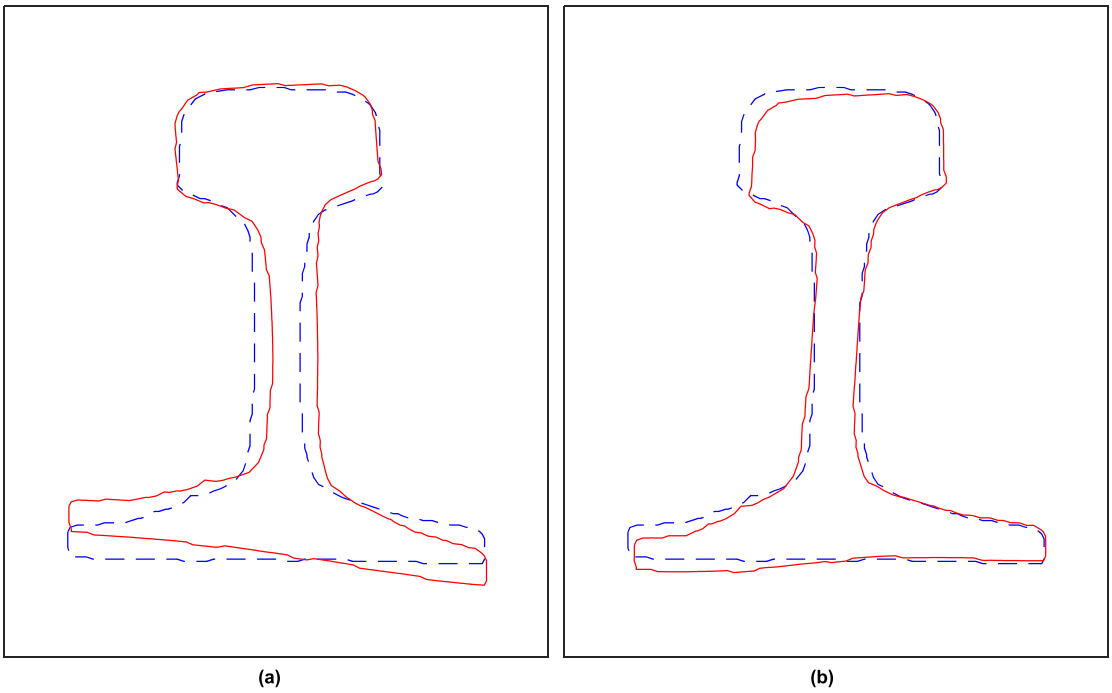

FIGURE 14. (a) First and (b) second web bending vibration modes identified from the PBM.

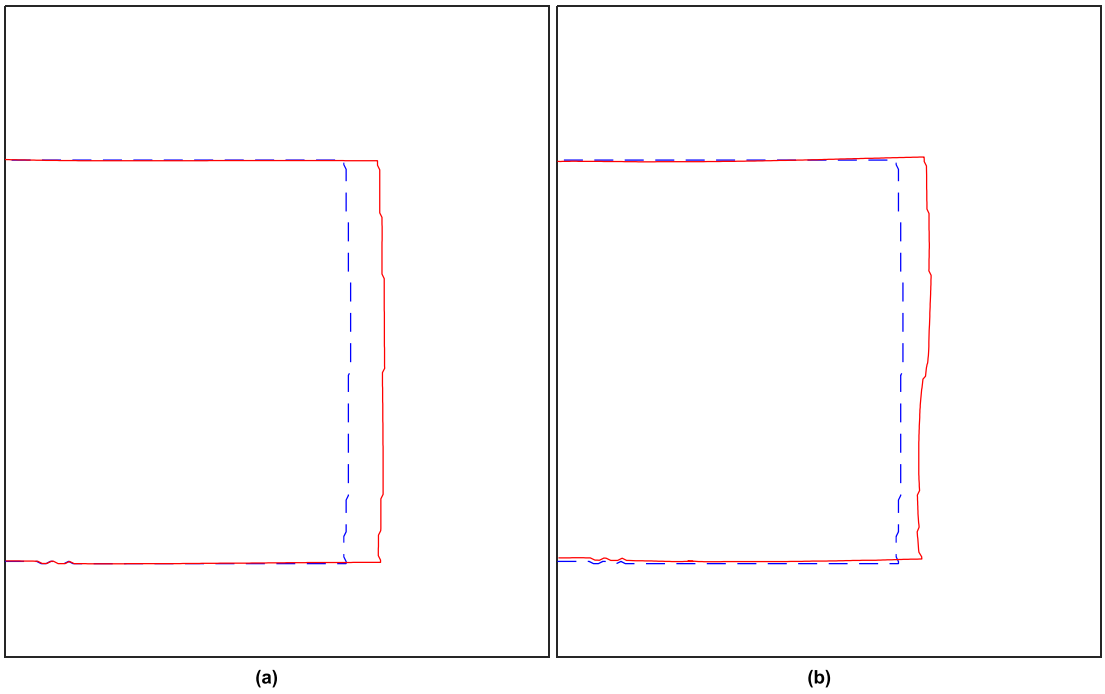

FIGURE 15. (a) First and (b) second longitudinal wave identified from the PBM.

these two modes. The recorded play rates are 20 and 5 FPS, respectively. The magnification factors are 2000 for Video 7 and 15000 for Video 8. Fig. 15 shows the frames with the largest deformations. The first and the second longitudinal waves are observed in these figures. The transverse motion of the rail appears along with the second longitudinal wave. These longitudinal motions should be analyzed when considering the wheel-rail or the rail-clamp vibration interactions.

Since there are a wide variety of rails depending on their applications, the rail parameters should be optimised based on their geometric properties including the head height, the bottom dimensions, and the web dimensions. The material used

for the rail shows wide variation depending on manufacturing parameters. The performance of the rail must be evaluated based on the vibration tests. Modal tests are widely used for the vibration tests of finite dimension structures. Although predicted using the waveguide method, the measurement of the vibration characteristics for the evaluation of the vibration transfer mechanism is difficult due to the insufficient resonant responses in the beam specimens. The proposed method can help provide significant information regarding the noise generation and the fatigue damage evaluations for specific rail samples.

V. CONCLUSION

In this study, the vibration modes of the rail were measured using the PBM method and compared to their predictions to verify the feasibility. To investigate the vibration generation mechanisms, the wave propagation characteristics of infinite-length rails were predicted using the WFE method. At a low frequency below 1 kHz, the vertical, the lateral the bending wave, the torsional wave, and the longitudinal wave were observed for the rail used in this study. The first and the second order web bending waves, the flapping wave mode and the second order longitudinal wave were observed at high frequencies, between 1 and 7 kHz. To identify the vibration modes using the PBM method, the cross-section and the side of the rail were recorded with a high-speed camera. The video was used to observe the motion at a high frequency, up to 7 kHz. To magnify the rail motion, a certain frequency range was determined, where the vibrations appear dominantly. The dispersion diagram of the rail was utilized in the measurement. The motion was magnified by applying a frequency band-pass filter. When a point force was applied at the center of the rail head in the vertical direction, the vertical bending wave and the flapping wave mode of the rail foot were observed. The lateral bending and the torsion waves were measured when a point force is applied on the rail head in the lateral direction. The local motion, which includes the first and second order web bending waves, was observed when a point force was applied on the rail foot in the vertical direction. The first and the second order longitudinal wave modes were observed from the excitation in the axial direction. Different mode shapes were measured using different frequency band-pass filters even if the excitations were identical. In this study, it was confirmed that the PBM method provides important information about the wave propagation mechanism and the vibration transfer mechanism on waveguide structures. The proposed method can be used to resolve the issues in the analysis of vibration transfer and noise generation especially for complex-shaped waveguides.

ACKNOWLEDGMENT

The authors are grateful to David J. Thompson at the Institute of Sound and Vibration Research, University of Southampton, for being allowed to use the software WANDS (Wave-Number-Domain FE-BE Software).

REFERENCES

[1] O. S. Salawu, "Detection of structural damage through changes in frequency: A review," *Eng. Struct.*, vol. 19, no. 9, pp. 718–723, Sep. 1997.
[2] O. Cakar and K. Y. Sanliturk, "Elimination of transducer mass loading effects from frequency response functions," *Mech. Syst. Signal Process.*, vol. 19, no. 1, pp. 87–104, 2005.
[3] J. M. M. Silva, N. M. M. Maia, and A. M. R. Ribeiro, "Cancellation of mass-loading effects of transducers and evaluation of unmeasured frequency response functions," *J. Sound Vib.*, vol. 236, no. 5, pp. 761–779, Oct. 2000.
[4] D. Feng and M. Q. Feng, "Experimental validation of cost-effective vision-based structural health monitoring," *Mech. Syst. Signal Process.*, vol. 88, pp. 199–211, May 2017.
[5] J. Baqersad, P. Poozesh, C. Niezrecki, and P. Avitabile, "Photogrammetry and optical methods in structural dynamics—A review," *Mech. Syst. Signal Process.*, vol. 86, pp. 17–34, Mar. 2017.
[6] P. Mazzoleni and E. Zappa, "Vision-based estimation of vertical dynamic loading induced by jumping and bobbing crowds on civil structures," *Mech. Syst. Signal Process.*, vol. 33, pp. 1–12, Nov. 2012.
[7] F. Cheli, P. Mazzoleni, M. Pezzola, E. Ruspini, and E. Zappa, "Vision-based measuring system for rider's pose estimation during motorcycle riding," *Mech. Syst. Signal Process.*, vol. 38, no. 2, pp. 399–410, Jul. 2013.
[8] J. Baqersad, C. Niezrecki, and P. Avitabile, "Extracting full-field dynamic strain on a wind turbine rotor subjected to arbitrary excitations using 3D point tracking and a modal expansion technique," *J. Sound Vib.*, vol. 352, pp. 16–29, Sep. 2015.
[9] J. Baqersad, C. Niezrecki, and P. Avitabile, "Full-field dynamic strain prediction on a wind turbine using displacements of optical targets measured by stereophotogrammetry," *Mech. Syst. Signal Process.*, vols. 62–63, pp. 284–295, Oct. 2015.
[10] M. N. Helfrick, C. Niezrecki, P. Avitabile, and T. Schmidt, "3D digital image correlation methods for full-field vibration measurement," *Mech. Syst. Signal Process.*, vol. 25, no. 3, pp. 917–927, 2011.
[11] J. Li, X. Xie, G. Yang, B. Zhang, T. Siebert, and L. Yang, "Whole-field thickness strain measurement using multiple camera digital image correlation system," *Opt. Lasers Eng.*, vol. 90, pp. 19–25, Mar. 2017.
[12] C. Liu, A. Torralba, W. T. Freeman, F. Durand, and E. H. Adelson, "Motion magnification," *ACM Trans. Graph.*, vol. 24, no. 3, pp. 519–526, 2005.
[13] H.-Y. Wu, M. Rubinstein, E. Shih, J. Guttag, F. Durand, and W. Freeman, "Eulerian video magnification for revealing subtle changes in the world," *ACM Trans. Graph.*, vol. 31, no. 4, pp. 1–8, 2012.
[14] N. Wadhwa, M. Rubinstein, F. Durand, and W. T. Freeman, "Phase-based video motion processing," *ACM Trans. Graph.*, vol. 32, no. 4, pp. 1–10, 2013.
[15] M. Rubinstein, "Analysis and visualization of temporal variations in video," Ph.D. dissertation, Dept. Elect. Eng. Comp. Sci., MIT, Cambridge, MA, USA, 2014.
[16] N. Wadhwa, M. Rubinstein, F. Durand, and W. T. Freeman, "Riesz pyramids for fast phase-based video magnification," in *Proc. IEEE Int. Conf. Comput. Photogr. (ICCP)*, May 2014, pp. 1–10.
[17] N. Wadhwa, "Revealing and analyzing imperceptible deviations in images and videos," Ph.D. dissertation, Dept. Elect. Eng. Comp. Sci., MIT, Cambridge, MA, USA, 2016.
[18] N. Wadhwa, J. G. Chen, J. B. Sellon, D. Wei, M. Rubinstein, R. Ghaffari, D. M. Freeman, O. Büyüköztürk, P. Wang, and S. Sun, "Motion microscopy for visualizing and quantifying small motions," *Proc. Nat. Acad. Sci. USA*, vol. 114, no. 44, pp. 11639–11644, 2017.
[19] M. Civera, L. Z. Fragonara, and C. Surace, "An experimental study of the feasibility of phase-based video magnification for damage detection and localisation in operational deflection shapes," *Strain*, vol. 56, Feb. 2020, Art. no. e12336.
[20] J. G. Chen, N. Wadhwa, Y.-J. Cha, F. Durand, W. T. Freeman, and O. Buyukozturk, "Modal identification of simple structures with high-speed video using motion magnification," *J. Sound Vib.*, vol. 345, pp. 58–71, Jun. 2015.
[21] A. Sarrafi, Z. Mao, C. Niezrecki, and P. Poozesh, "Vibration-based damage detection in wind turbine blades using phase-based motion estimation and motion magnification," *J. Sound Vib.*, vol. 421, pp. 300–318, May 2018.
[22] K. Knothe, Z. Strzyzakowski, and K. Willner, "Rail vibrations in the high frequency range," *J. Sound Vib.*, vol. 169, no. 1, pp. 111–123, Jan. 1994.
[23] M. Oregui, Z. Li, and R. Dollevoet, "An investigation into the vertical dynamics of tracks with monoblock sleepers with a 3D finite-element model," *Proc. Inst. Mech. Eng. F, J. Rail Rapid Transit*, vol. 230, no. 3, pp. 891–908, Mar. 2016.

[24] P. Zhang, S. Li, A. Núñez, and Z. Li, "Multimodal dispersive waves in a free rail: Numerical modeling and experimental investigation," *Mech. Syst. Signal Process.*, vol. 150, Mar. 2021, Art. no. 107305.
[25] R. Cettour-Janet, A. Barbarulo, F. Letourneaux, and G. Puel, "An Arnoldi reduction strategy applied to the semi-analytical finite element method to model railway track vibrations," *Mech. Syst. Signal Process.*, vol. 116, pp. 997–1016, Feb. 2019.
[26] L. Gavrić, "Computation of propagative waves in free rail using a finite element technique," *J. Sound Vib.*, vol. 185, no. 3, pp. 531–543, 1995.
[27] I. I. Setshedi, P. W. Loveday, C. S. Long, and D. N. Wilke, "Estimation of rail properties using semi-analytical finite element models and guided wave ultrasound measurements," *Ultrasonics*, vol. 96, pp. 240–252, Jul. 2019.
[28] C. M. Nilsson, "Waveguide finite elements applied on a car tyre," Ph.D. dissertation, Superseded Dept., Aeronaut. Vehicle Eng., KTH, Stockholm, Sweden, 2004.
[29] C.-M. Nilsson, C. J. C. Jones, D. J. Thompson, and J. Ryue, "A waveguide finite element and boundary element approach to calculating the sound radiated by railway and tram rails," *J. Sound Vib.*, vol. 321, pp. 813–836, Apr. 2009.
[30] J. Ryue, D. J. Thompson, P. R. White, and D. R. Thompson, "Investigations of propagating wave types in railway tracks at high frequencies," *J. Sound Vib.*, vol. 315, pp. 157–175, Aug. 2008.
[31] J. Ryue, D. J. Thompson, P. R. White, and D. R. Thompson, "Decay rates of propagating waves in railway tracks at high frequencies," *J. Sound Vib.*, vol. 320, pp. 955–976, Mar. 2009.
[32] J. Ryue, S. Jang, and D. J. Thompson, "A wavenumber domain numerical analysis of rail noise including the surface impedance of the ground," *J. Sound Vib.*, vol. 432, pp. 173–191, Oct. 2018.
[33] H. Kim and J. Ryue, "Sound radiation from strip plates with longitudinal stiffeners using waveguide finite and boundary element methods," *J. Mech. Sci. Technol.*, vol. 28, pp. 2527–2534, Jul. 2014.
[34] H. Kim, J. Ryue, D. Thompson, and A. Müller, "Prediction of radiation ratio and sound transmission of complex extruded panel using wavenumber domain unite element and boundary element methods," *J. Phys., Conf. Ser.*, vol. 744, no. 1, 2016, Art. no. 012144.
[35] H. Kim, J. Ryue, D. J. Thompson, and A. D. Müller, "Application of a wavenumber domain numerical method to the prediction of the radiation efficiency and sound transmission of complex extruded panels," *J. Sound Vib.*, vol. 449, pp. 98–120, Jun. 2019.
[36] C. M. Nilsson, A. N. Thite, C. J. C. Jones, and D. J. Thompson, "Estimation of sound transmission through extruded panels using a coupled waveguide finite element-boundary element method," in *Noise and Vibration Mitigation for Rail Transportation Systems*. Berlin, Germany: Springer, 2008, pp. 306–312.
[37] U. Orrenius and S. Finnveden, "Calculation of wave propagation in rib-stiffened plate structures," *J. Sound Vib.*, vol. 198, no. 2, pp. 203–224, Nov. 1996.
[38] I. Prasetiyo, "Investigation of sound transmission in lightweight structures using a waveguide finite element/boundary element approach," Ph.D. dissertation, ISVR, Univ. Southampton, Southampton, U.K., 2012.
[39] C. M. Nilsson and C. J. Jones, "Theory manual for WANDS 2.1 wave number domain FE-BE software for structures and fluids," ISVR, Univ. Southampton, Southampton, U.K., Tech. Memorandum 975, 2007.
[40] A. Sarrafi, "Structural dynamics identification via computer vision approaches," Ph.D. dissertation, Univ. Massachusetts Lowell, Lowell, MA, USA, 2019.
[41] E. P. Simoncelli, W. T. Freeman, E. H. Adelson, and D. J. Heeger, "Shiftable multiscale transforms," *IEEE Trans. Inf. Theory*, vol. 38, no. 2, pp. 587–607, Mar. 1992.
[42] E. P. Simoncelli and W. T. Freeman, "The steerable pyramid: A flexible architecture for multi-scale derivative computation," in *Proc. Int. Conf. Image Process.*, 1995, pp. 444–447.

HYUNGJUN KIM received the B.S. degree in ocean engineering and in mechanical and automotive engineering and the M.S. and Ph.D. degrees in ocean engineering from the University of Ulsan, in 2012, 2014, and 2020, respectively. He currently holds a post doctoral position at the Acoustics and Vibration Laboratory, Hanyang University. His research interests include vibro-acoustic analysis of complex shaped waveguide structures, health monitoring, and image or signal processing.

YOUNGBEEN CHUNG received the B.S. degree in mechanical engineering from Hanyang University, in 2019, where she is currently pursuing the Ph.D. degree with the Acoustics and Vibration Laboratory. Her research interests include vibro-acoustic analysis of advanced structural elements, health monitoring, signal processing, and AI technique.

JIE JIN received the B.S. degree in mechanical engineering from the Liaoning University of Technology, in 2012, and the Ph.D. degree from Hanyang University, in 2021. From 2012 to 2015, he worked at Beijing-Hyundai Motor Technical Center. He is currently an Assistant Professor with the School of Electromechanical and Automotive Engineering, Yantai University. His research interests include structure vibration, railway vibration, and passive vibration damping using damper.

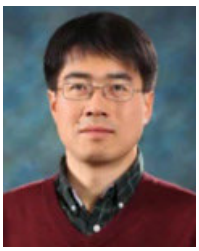

JUNHONG PARK (Member, IEEE) received the B.S. and M.S. degrees from the Korea Advanced Institute of Science and Technology (KAIST), in 1991 and 1993, respectively, and the Ph.D. degree from Purdue University, in 2002. From 1993 to 1998, he worked at Samsung Electronics Company Ltd. He is currently a Professor with the Department of Mechanical Engineering, Hanyang University. His research interests include signal processing, wave analysis, and noise control for improving damping, or machine learning performance, including mechanical issue.